Paper No. 16

SIMULATION OF MARTIAN EOLIAN PHENOMENA IN THE ATMOSPHERIC WIND TUNNEL

J. D. Iversen, *Iowa State University;* R. Greeley, *University of Santa Clara;* J. B. Pollack, *NASA', Ames Research Center;* and B. R. White, *Iowa State University*

ABSTRACT

Comparisons are made between the Mariner 9 photographs of wake streaks associated with craters on Mars, and experiments conducted in an atmospheric boundary layer wind tunnel. The appropriate modeling parameters are developed and discussed. The results of threshold speed experiments for a variety of particle densities and diameters are presented and used to predict threshold speeds on Mars.

The Atmospheric Wind Tunnel

Several wind tunnel installations have been constructed to investigate the effects of wind on sand and soil movement. The primary facility for studying the transport of sand by wind was that of Bagnold[1]. Experiments conducted in his wind tunnel resulted in definitive curves and equations for threshold friction speed and mass transport of sand due to wind. Another facility used mostly for studying wind erosion of soil is described by Chepil and Woodruff[2]. Other wind tunnels for the study of soil and sand transport by wind have been built[3,4]. Since the atmosphere on Mars is much less dense than on Earth, facilities were proposed in which Martian dust storms could be simulated under reduced pressure[5,6]. One wind tunnel was constructed and threshold speeds were determined at pressures as low as those on the surface of Mars[7-9]. Although an exact experimental determination of threshold speed should be performed in a low-density wind tunnel, deposition and flow patterns over surface features can be modeled to some extent in a normal atmospheric boundary-layer wind tunnel[6], if close attention is paid to satisfying appropriate modeling parameters and to the wind tunnel boundary layer configuration.

The structure of the turbulent planetary boundary layer on earth has been studied extensively[10,11]. Jensen[12] and others have observed that the lower portion of the planetary boundary layer (in a neutrally stratified atmosphere) follows the logarithmic law

$$\frac{u(z)}{u_*} = \frac{1}{k} \ln \frac{z}{z_o} \qquad (1)$$

where u_* is the friction velocity and k is von Kármán's constant ($k \simeq 0.4$). Jensen showed that for simulation of the atmospheric boundary layer, the roughness parameter for the wind-tunnel floor must scale with the roughness parameter in nature, i.e.,

$$\frac{z_{o_M}}{z_o} = \frac{L_m}{L} .$$ (2)

Most investigators have relied on the long test section to simulate the turbulent boundary layer profile so the model is immersed in the boundary layer[13,14]. However, it is possible, although perhaps not as desirable, to produce thick boundary layers with the proper scaled velocity profiles in shorter test sections[15-17]. Effects due to a nonneutral atmosphere (stable or unstable) can be simulated to some extent by cooling or heating the tunnel floor[13].

Modeling of Martian Eolian Phenomena

The deposition and erosion of fine particles blowing over a complex terrain presents a very intricate phenomenon to attempt to physically simulate on a smaller geometric scale. The erodibility of soil or sand is a complicated function of mean wind speed, frequency and intensity of gusts, and particle size distribution, density and shape, and topographic surface roughness. An optimum size occurs, for soil on earth, for which the threshold speed is a minimum. On Mars, the optimum particle size and threshold speeds are predicted to be larger[18], mostly because of lower atmospheric density, although terminal speeds for like particles are predicted to be about the same as on earth[5].

The list of important physical parameters in the eolian process includes:

D_p particle diameter

L   major terrain feature length (such as crater diameter)

ℓ all other terrain feature lengths

z_o roughness length

z_o' roughness length in saltation

h   specified altitude for reference speed

L^* Monin-Obhukov length (atmospheric stability parameter)

λ ripple wavelength

U(h) reference wind velocity

192

U_F particle terminal speed

u_* friction speed

u_{*_t} threshold friction speed

ρ atmospheric density

ρ_p particle density

ν kinematic viscosity

t time (duration of phenomenon)

e coefficient of restitution

These parameters can be arranged in the form of dimensionless similitude parameters.

1. $\dfrac{D_p}{L}$ length ratio

2. $U(h)/U_F$ reference to particle terminal speed ratio

3. $[U(h)]^2/gL$ Froude number

4. e coefficient of restitution

5. ℓ/L topographic geometric similarity

6. z_0/L roughness similitude

7. z_0'/L roughness similitude in saltation

8. h/L reference height similitude

9. z_0/L^* stability parameter

10. λ/L ripple length similitude

11. U_F/U_{*_t} particle property similitude

12. $U_{*_t}D_p/\nu$ particle friction Reynolds number

13. u_*/u_{*_t} friction speed ratio

14. ρ/ρ_p density ratio

15. $U(h)t/L$ time scale

The first four of these parameters have been suggested by Gerdel and Strom[19] as the scaling parameters of primary im-

193

portance in modeling accumulation of wind-driven snow. Many of the other parameters are interrelated and so satisfaction of some of the parameters will result in automatic satisfaction of others. For example, the roughness height in saltation, z_o', has been assumed by different investigators to be proportional to particle diameter[20] (as is z_o, if no nonerodible roughness elements are present[1]), to ripple wavelength[1], or to be a function of particle terminal speed[21] ($z_o' \sim U_F^2/g$). Thus parameter number 7 is just a constant times number 1 in the first case and number 10 in the second case. In the third case, since[1]

$$u_{*_t} = A \sqrt{\frac{\rho_p g D_p}{\rho}} \,, \tag{3}$$

the parameter z_o'/L would be related to parameters 1, 11, and 14

$$\frac{z_o'}{L} \sim \frac{U_F^2}{gL} = A^2 \frac{\rho_p}{\rho} \left(\frac{D_p}{L}\right)\left(\frac{U_F}{u_{*_t}}\right)^2 \tag{4}$$

Some of the listed modeling parameters may be combined by using the equation of motion for the particle. Since the flow pattern near a crater and in the crater wake is related to the crater diameter, the vertical equation of motion, for example, is made dimensionless by using the dimensionless variables $\bar{Z} = Z/D_c$ (where Z is the vertical displacement) and $\bar{t} = U(h)t/D_c$. The equation becomes

$$d^2\bar{Z}/d\bar{t}^2 = -\, 3/4 C_D\left(\frac{\rho D_c}{\rho_p D_p}\right) \bar{V}(\bar{W} - d\bar{Z}/d\bar{t}) - gD_c/U(h)^2 \tag{5}$$

where $\bar{V}$ is the dimensionless relative speed and $\bar{W}$ the dimensionless vertical air speed. Thus the dimensionless motion is a function of the three parameters $\rho D_c/\rho_p D_p$, $U(h)^2/gD_c$, and the particle Reynolds number.

Consider the modeling parameters:

1. $\rho D_c/\rho_p D_p$. By varying particle density and diameter and the crater diameter, this parameter can be varied from about 0.8 to 3. On Mars, this parameter would vary in value from about 1 for a 100 meter diameter crater to 100 for a 10 kilometer crater.

2. $U(h)/U_F$. Since the threshold friction speed u_* is proportional to the reference velocity $U(h)$, providing geometry (including roughness) is exactly modeled, the ratio of reference velocity $U(h)$ to terminal speed U_F will be modeled exactly if the ratio u_*/U_F is satisfied and if h/L is satisfied.

3. $[U(h)]^2/gL$. The Froude number cannot always be satisfied in the wind tunnel without having a tunnel speed far below threshold speed. It is desirable to make it as small as possible. Again since u_* is proportional to $u(h)$, this is equivalent to requiring a modeling

194

material with as small a threshold speed as possible.
The value of this parameter varies from 10 to 150 in
the wind tunnel, and from approximately 20 for a
100 meter diameter crater to 0.2 for a 10 kilometer
crater.

4. e. The coefficient of restitution is satisfied if
model and atmospheric materials have equivalent elastic
properties.

5. ℓ/L. Topographic features should be scaled exactly to
satisfy this criterion. At large distances upstream
from the region of interest, it is probably only neces-
sary to have equivalent scaled aerodynamic roughness.

6. z_0/L. The aerodynamic roughness should, in general, be
to scale[12]. Except for those craters surrounded by
large-scale ejecta or other rough surface features,
this is probably small on Mars. If the corresponding
model surface in the wind tunnel is too smooth, it may
be necessary to distort this parameter in order to ob-
tain a turbulent boundary layer. It is important at the
same time, to insure that the ratio h/L be satisfied.

7. Z_0'/D_c. If the equivalent roughness height in saltation
Z_0' is proportional to particle diameter, this parameter
obviously cannot be satisfied on the laboratory scale
model, since such fine particles would have a very high
threshold speed. Also, if introduced into the air
stream, the particles would go into suspension and the
saltation process would not occur. Calculations of
saltation trajectory, however, show that the maximum
height during saltation would be several times larger on
Mars than on Earth, just as the saltation height on
Earth is several times as large in air as it is in water.
If the equivalent roughness Z_0' is proportional to
U_F^2/g, then z_0'/D_c is proportional to $\rho_p D_p / \rho D_c$, the in-
verse of the first parameter.

8. h/L. The reference height h at which the reference
speed is measured should be located within the
logarithmic portions of the wind tunnel and atmos-
pheric boundary layers.

9. z_0/L^*. With a 'naturally' developed boundary layer in
the wind tunnel, a boundary layer velocity profile is
achieved which corresponds to a neutrally stratified
atmosphere, for which the Monin-Obhukov length L^* is
infinite and the ratio z_0/L^* is zero. A finite value
of L^* is achieved in the wind tunnel by heating or
cooling the floor to obtain unstable or stable
stratification. Another way of obtaining a nonneutral
velocity profile in the wind tunnel (but perhaps not
correct modeling of turbulence characteristics) would
be by means of shear fences, graded grids, or the
like[16].

10. λ/L. The relative ripple length may be related to

z_0'/L and the same comments apply.
11. U_F/u_{*_t} and 12. $u_{*_t}D_p/\nu$. As will be shown later, for a given condition such as for a modeling particle of diameter corresponding to minimum threshold speed, these two parameters would have the same values as for minimum threshold speed material on Mars.
13. u_*/u_{*_t}. The manner in which particles are transported and, in particular, the amount of material which is moved is a function of this ratio. Thus, in order to keep u_* as small as possible because of the Froude number, the threshold friction speed of the particle should be small.
14. $U(h)t/L$. The time scale in the wind tunnel is much shorter than the time necessary for pattern development on Mars since the characteristic time is the ratio of characteristic length L to reference velocity $U(h)$. The time necessary for pattern development on Mars can thus be predicted from wind tunnel tests.
15. A Reynolds number $U(h)L/\nu$ may or may not be an important modeling parameter. For turbulent flows over sharp-edged features, the flow is relatively independent of Reynolds number. The critical model Reynolds number (above which effects are independent of Reynolds number) depends upon model shape. If the model is too streamlined so that the test Reynolds number is below the critical, the model may have to be distorted by roughening the surface, creating sharper edges, etc. in order to lower the critical Reynolds number. Snyder[22] quotes critical Reynolds number for sharp-edged cubes of 11,000 and 79,000 for a hemisphere-cylinder. In the current tests, Reynolds numbers based on crater diameter were generally above these values for sharp-rimmed model craters.

The listed parameters are easier to satisfy or will come closer to satisfaction in the one atmosphere wind tunnel than in the low density tunnel. Thus, for modeling eolian features on Martian topography, the low density wind tunnel should not be used.

Threshold Speed Experiments

Two series of experiments have been initiated in atmospheric wind tunnels. The first series of tests is designed to gain additional fundamental knowledge about properties of saltating materials such as equivalent roughness height in saltation, ripple wavelength, and threshold friction speed. Results of tests for determining threshold friction speeds for a variety of particle sizes and densities are shown in Figs. 1 and 2. As Bagnold[1] discovered, an optimum particle size occurs for which threshold speed is a minimum, corresponding to a certain value of particle friction Reynolds number. The value of optimum diameter decreases as particle density increases with the

diameter ratio inversely proportional to the density ratio to the one-third power. The minimum threshold speed ratio should be directly proportional to the one-third power of the density ratio. Limited data in Figs. 1 and 2 comparing copper particles and glass spheres corroborate these trends.
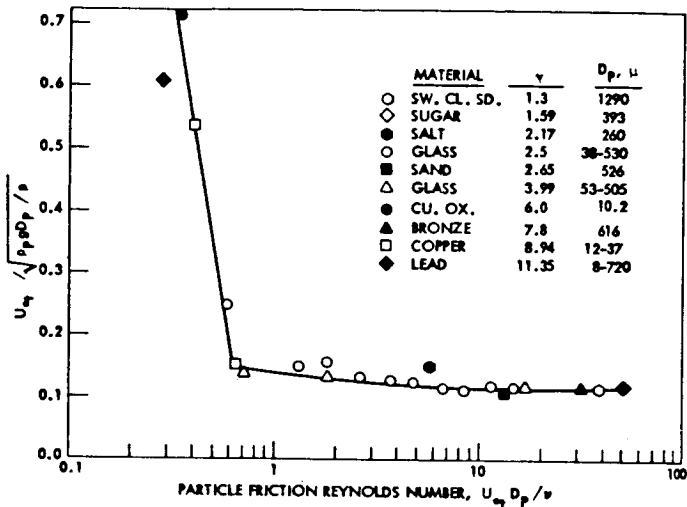

	MATERIAL	γ	D_p, μ
O	SW. CL. SD.	1.3	1290
◇	SUGAR	1.59	393
●	SALT	2.17	260
O	GLASS	2.5	38–530
■	SAND	2.65	526
△	GLASS	3.99	53–505
●	CU. OX.	6.0	10.2
▲	BRONZE	7.8	616
□	COPPER	8.94	12–37
◆	LEAD	11.35	8–720

Fig. 1. Threshold speed parameter ratio vs particle friction Reynolds number.
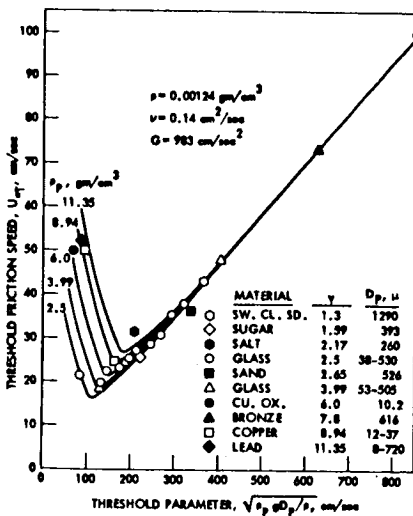
Fig. 2. Threshold friction speed vs threshold parameter.

197

In Fig. 1 the curve of Bagnold's parameter $A = u_{*_t}/\sqrt{\rho_p g D_p/\rho}$ vs particle friction Reynolds number $B = u_{*_t} D_p/\nu$ should be a universal curve as long as the surface over which the wind is blowing is composed only of the erodible particles in question. The solid lines in Fig. 2 are based on the single curve in Fig. 1. Part of the small scatter in the data could be attributed to particle shape.

From the expressions for A and B the threshold friction speed u_{*_t} and particle diameter D_p can be estimated for any values of density ratio, ρ/ρ_p, gravitational acceleration, g, and kinematic viscosity, ν, from Eqs. (1) and (2).

$$u_{*_t} = A^{2/3}(\rho_p g \nu B/\rho)^{1/3} \tag{6}$$

$$D_p = (B\nu/A)^{2/3}(\rho/\rho_p g)^{1/3} \tag{7}$$

The point on the curve in Fig. 1 where the relatively sharp break occurs (A = 0.146 and B = 0.68) corresponds to the minimum threshold friction speed. For values typical of a one-atmosphere wind tunnel, the values of minimum u_{*_t} and corresponding D_p were calculated for a range of values of particle density, using Eqs. (6) and (7). The results are shown in Fig. 3. If a modeling material is chosen to correspond to minimum threshold speed, then it is evident that if minimum diameter is desired, then the material should be of high density. However, materials of lighter density will result in somewhat lower minimum threshold speeds. Parameter number 1, for given values of A and B, is proportional to $(\rho/\rho_p)^{2/3}$. Thus, lighter materials will result in larger values of this parameter.

Fig. 3.
Variation with density of particle diameter and threshold friction speed for minimum threshold speed.

198
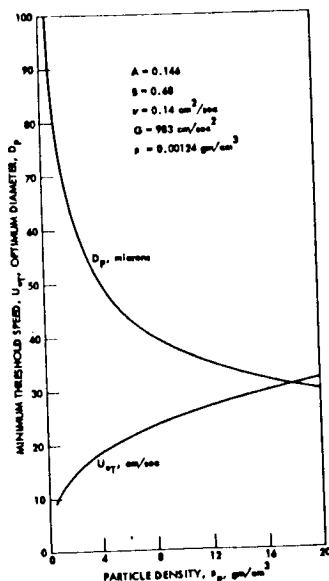
The terminal speed to threshold friction speed ratio U_F/u_{*_t} can be written as a function of A and terminal speed drag coefficient C_{D_F}. However, C_{D_F} is a function of $U_F D_p/\nu =$ $(U_F/u_{*_t})u_{*_t}D_p/\nu = (U_F/u_{*_t})B$. Thus, for a given A and B corresponding to a particular point on the curve in Fig. 1, the ratio U_F/u_{*_t} is uniquely determined and would have the same values on Mars as in the wind tunnel. It follows that

$$\frac{U_F}{u_{*_t}} = \frac{2/A}{\sqrt{3C_{D_F}}} \tag{8}$$

where $\quad C_{D_F} = C_{D_F}(BU_F/u_{*_t})$

Effect of Particle Lift on Threshold Speed

Although some investigators have ignored the effect of particle lift in attempting to predict threshold friction speed, the effect of lift is apparently important. Bagnold[23,24] has stated that the initial upward acceleration of a particle (not struck by another particle) from the bed is due to a lift-force but that the lift force becomes very small shortly after the particle has lifted off the bed. The lift force is due to the very high mean velocity gradient very near the surface. Experimental values of lift on hemispheres lying on a surface and immersed in a fluid were obtained by Chepil[25] and Einstein and El-Samni[26]. In both cases the lift and drag forces were found to be of the same order of magnitude. However, the measurements of lift and drag in both cases were made at relatively high Reynolds number (diameters ranged from 1.27 cm to 6.86 cm in air and water), in fully turbulent flow, whereas the threshold values of u_* occur for values of particle friction Reynolds numbers in the laminar sublayer and transition ranges. According to Schlichting[27], for a closely packed sand surface roughness, the surface is aerodynamically smooth if the particle friction Reynolds number, u_*D_p/ν is 5 or less, and a laminar sublayer exists adjacent to the surface. If the particle friction Reynolds number is greater than 70, the particles would be larger than a laminar sublayer if one could exist, and the boundary layer is fully turbulent. Between these values is a transition range in which the velocity profile is still a function of u_*D_p/ν.

An effective lift coefficient at threshold was calculated from the data depicted in Figs. 1 and 2 with the use of a mean velocity profile equation valid throughout a turbulent boundary layer with a laminar sublayer as presented by Walz[28]. This effective lift coefficient would include any packing factor or turbulence factor as used by Chepil[29]. It is assumed (as did Chepil[29]) that the lift acts at the center of the spherical particle and the drag acts at a distance of $D_p/6$ above the

sphere center, which is resting atop other spheres of the same diameter. Equating opposing moments due to lift, drag, and weight results in

$$u_{*_t} = 0.3728 \sqrt{\frac{\rho_p g D_p}{\rho} \left[\frac{1}{1 + \frac{C_L}{9.6} \left(\frac{u}{u_*}\right)^2} \right]} \qquad (9)$$

The substitution of Walz's velocity profile, evaluated at $z = D_p$, resulted in the value of lift coefficient shown as curve 1 in Fig. 4. For values of $u_* D_p/\nu$ greater than 5, curve 1 would not be expected to be valid, since Walz's equation implies an aerodynamically smooth surface. The lift coefficient was recalculated for the transition region (using Schlichting's velocity profile[24], his Fig. 20.21), shown as curve 2. His profile does not account for remnants of the laminar sublayer in the transition region, however, and would not be valid until $u_* D_p/\nu = 70$. Thus curve 3 is presented, an interpolated curve, which is
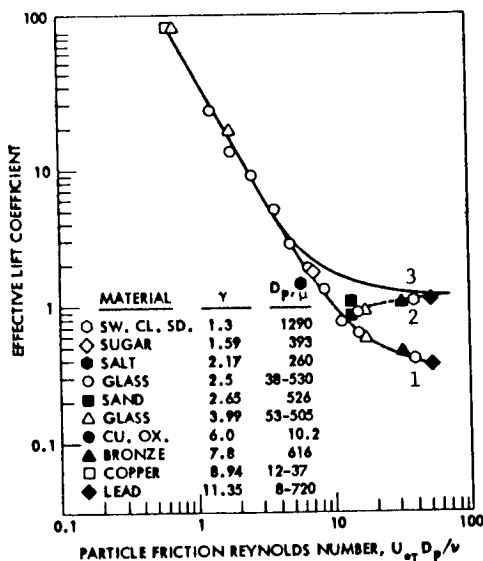

Fig. 4. Calculated effective lift coefficient at threshold.

probably closer to the actual value of effective lift coefficient. As Bagnold[24] has recently pointed out, saltation can occur in purely laminar motion, so that saltation cannot be attributed to turbulence. Thus the assumption of a lift force, initiating saltation in the absence of the particle being struck by another, appears to be valid. The lift would be very small, however, as soon as the particle rises above the region of very high shear near the surface.

200

Whether or not the particle returns to the surface in a typical saltation trajectory, or becomes suspended due to fluid turbulence, depends upon the ratio of terminal speed to threshold friction speed, U_F/u_{*_t}, and the friction speed to threshold ratio, u_*/u_{*_t}. Since the vertical component of turbulent fluctuation is of the same order as u_* near the surface, if U_F/u_{*_t} is near unity, then much of the material will be affected by turbulence at speeds very near threshold. Conversely, if U_F/u_{*_t} is large, u_*/u_{*_t} would also have to be large in order for turbulence to greatly affect particle motion. At minimum threshold speed, corresponding to $u_{*_t}D_p/\nu \simeq 0.68$, the ratio U_F/u_{*_t} is 1.6. The ratio increases with $u_{*_t}D_p/\nu$, and is 9.4 at $u_{*_t}D_p/\nu = 10$, for example.

Effect of Nonerodible Roughness

From Fig. 4 it would appear the lift coefficient would change much less rapidly for Reynolds numbers greater than 70, and in fact, for fully turbulent flow, should be a function only of mean velocity gradient. This would also appear to be true from Fig. 1 where it is seen that Bagnold's coefficient A approaches a constant value for Reynolds numbers above 5 which implies a constant value of lift coefficient for Reynolds numbers greater than 70. Thus, for $u_{*_t}z_0/\nu \geq 70/30$, if a reference velocity for computing lift coefficient of $u = \frac{u_*}{0.4} \ln(\frac{D_p}{z_0})$ is chosen and if the lift coefficient is solved for by letting $A = 0.117$ (the limit value in Fig. 1) and $D_p/z_0 = 30$, an equation for u_{*_t} as a function of D_p/z_0 results (for fully rough flow):

$$A = \frac{u_{*_t}}{\sqrt{\rho_p g D_p/\rho}} = \frac{0.373}{\sqrt{1 + 0.776[\ln(1 + D_p/z_0)]^2}} \tag{10}$$

For no nonerodible roughness, $D_p/z_0 = 30 (u_{*_t}D_p/\nu \geq 70)$, and $A = 0.117$. If large nonerodible roughness elements are present, then the equivalent roughness height z_0 becomes greater than $D_p/30$ and Bagnold's coefficient A increases according to Eq. (10). It has been previously observed that nonerodible roughness elements do greatly increase the value of the coefficient[2]. To test the validity of Eq. (10), values of threshold friction speed for several materials were determined for values of nonerodible equivalent roughness heights z_0 of 0.0104 cm and 0.338 cm. The results of the experiments are shown in Fig. 5. Although there is quite a bit of data scatter, the results seem to substantiate the form of Eq. (10). The letters NNR in Fig. 5 signify that no nonerodible roughness elements were present in those tests and that the ratio D_p/z_0 is 30 (or slightly higher in the transition range). Figure 6 shows the threshold friction speed as a function of particle diameter for one of the test materials (heavy glass spheres). The lower curve is derived from the curve of Fig. 1 and the other curves from Eq. (10). Again the trend of Eq. (10) seems to be substantiated by the experimental results.
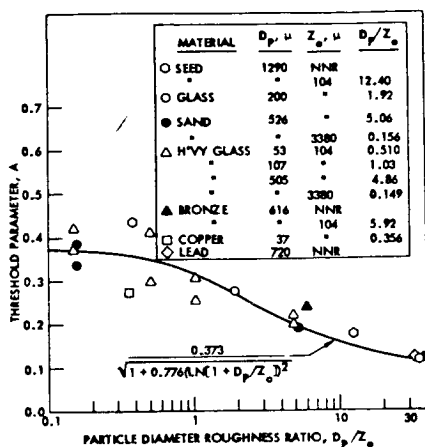
MATERIAL	D_p, μ	Z_o, μ	D_p/Z_o
○ SEED	1290	NNR	
•		104	12.40
○ GLASS	200	"	1.92
• SAND	526	"	5.06
•		3380	0.156
△ H'VY GLASS	53	104	0.510
•	107	"	1.03
•	505	"	4.86
•		3380	0.149
▲ BRONZE	616	NNR	
•		104	5.92
□ COPPER	37	"	0.356
◇ LEAD	720	NNR	

$$\frac{0.373}{\sqrt{1 + 0.776(LN[1 + D_p/Z_o])^2}}$$

Fig. 5. Threshold speed parameter ratio vs ratio of particle diameter to nonerodible roughness height.

NON-ERODIBLE ROUGHNESS HEIGHT

△ NO NON-ERODIBLE ROUGHNESS
○ Z_o = 0.0104 cm
▲ Z_o = 0.338 cm

ρ = 0.00124 gm/cm^3
ρ_p = 3.99 gm/cm^3
ν = 0.14 cm^2/sec
G = 983 c/s^2

Z_o, cm
0.338
0.15
0.05
0.0104
0.003
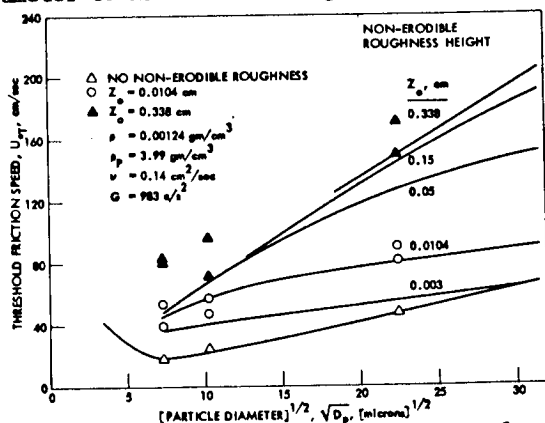
Fig. 6. Threshold friction speed as a function of particle diameter including effect of nonerodible roughness.

Predicted Threshold Speeds on Mars

With values of kinematic viscosity $\nu = 10.8$ cm^2/sec, gravitational acceleration g = 375 cm/sec^2, and atmospheric-to-particle density ratio of 4.21×10^{-6}, the curve of Fig. 1 was used to calculate threshold friction speeds on Mars, assuming that that curve also holds in the Martian atmosphere, with the use of Eqs. (6) and (7). Equation (10) was also used to calculate Martian values of threshold friction speed for several values of nonerodible roughness height z_o. These calculations are presented in Fig. 7. The minimum threshold friction speed, for no nonerodible roughness, is about 240 cm/sec, corresponding to a particle diameter of about 305 microns.
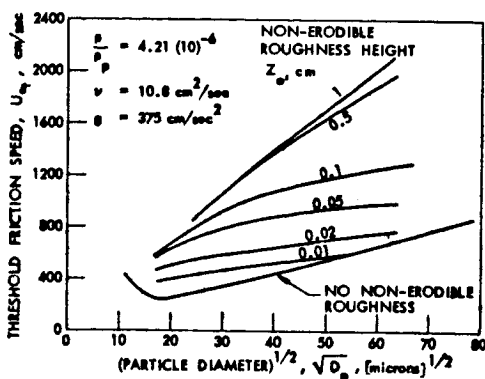
202

Fig. 7. Predicted threshold friction speed on Mars as a function of particle diameter.

The geostrophic wind at threshold, corresponding to the minimum value of threshold speed in Fig. 7 was calculated with the help of Csanady's drag coefficients for the diabatic Ekman layer[30], assuming that his results hold for the Martian atmosphere. For a latitude of 60° and an unstable atmosphere (Lettau number = 10^9), the minimum value of geostrophic wind is predicted to be 120 m/sec. The geostrophic winds at threshold would be slightly higher for a neutrally stratified atmosphere. It is apparent that very high winds are required for particle pick-up on the Martian surface. The corresponding minimum geostrophic wind at threshold on Earth would be on the order of 7.5 m/sec.

Modeling of Martian Eolian Features

The second series of tests concerns the modeling of eolian processes on Mars which have resulted in streaks emanating in a downstream direction from many of the craters. Figure 8 shows one of the Martian craters with the associated wake streak. The wind pattern over the crater would be similar to wind patterns observed over protuberances in boundary layers with small height to diameter ratios in laboratory scale tests on earth[31-33]. A horseshoe vortex is wrapped around the leading edge of the crater with the trailing vortices emanating downstream from the crater sides. The tangential component of velocity in each trailing vortex is outward away from the wake centerline near the surface and inward above the vortex cores. The axial velocity components near the surface just behind the downstream crater rim are minimal on the wake centerline with maximum velocities on either side of the wake of greater magnitude than outside the wake. Further downstream the two maxima merge, and the maximum speed in the wake is then on the centerline.
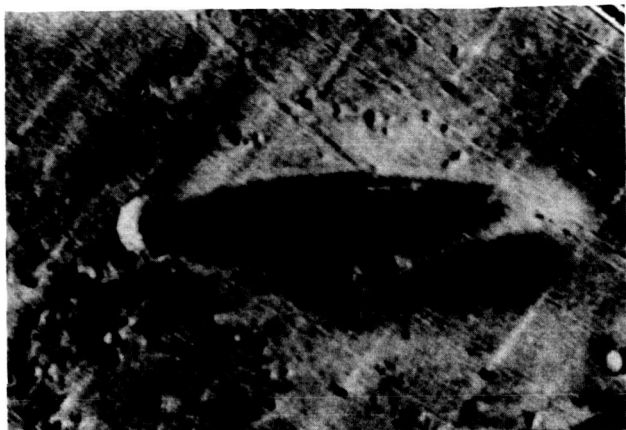
203

Fig. 8. Mariner-9 photograph — Mars crater with associated wake streak.

Figure 9 shows the results of a wind tunnel test over a model 30 cm diameter crater performed at a freestream speed of 675 cm/sec. Prior to the test, 393 micron diameter sugar particles were distributed evenly to a depth of 1 cm. The dark area in the crater wake represents the area cleared of particles because of the relatively high speed near the surface in the wake region. Except for the triangular area of material just downstream of the trailing rim, the cleared area bears a distinct resemblance to the Mariner 9 photo in Fig. 8. The values of the modeling parameters in this experiment were $U_\infty^2/gD_c = 15.41$, $U_F/u*_t = 10.10$, $U_\infty/U_{\infty_t} = 0.995$, and $\rho D_c/\rho_p D_p = 0.644$.
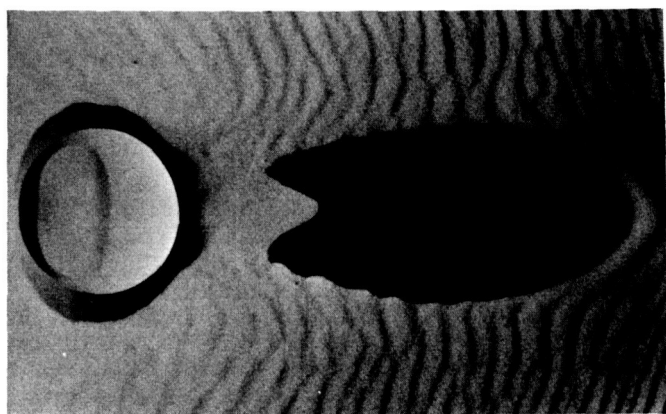

Fig. 9. Wind tunnel model crater with wake streak, $U_\infty^2/gD_c = 15.41$.

204

Another Mariner 9 photograph is shown in Fig. 10 with an apparent bi-lobate pattern in the crater wake, probably caused by the aforementioned two axial velocity maxima. The wind tunnel photograph in Fig. 11 depicts a very similar bi-lobate pattern, with clear area on either side of the wake and deposited material in the wake center. Prior to the test, no material was on the floor. Heavy glass spheres 107 micron average diameter were released from the tunnel ceiling upstream of the crater model. The modeling parameters' were $U_\infty^2/gD_c = 6.6$, $U_F/u_{*_t} = 3.5$, $U_\infty/U_{\infty_t} = 0.673$, ($U_\infty = 441$ cm/sec), and $\rho D_c/\rho_p D_p = 0.739$.

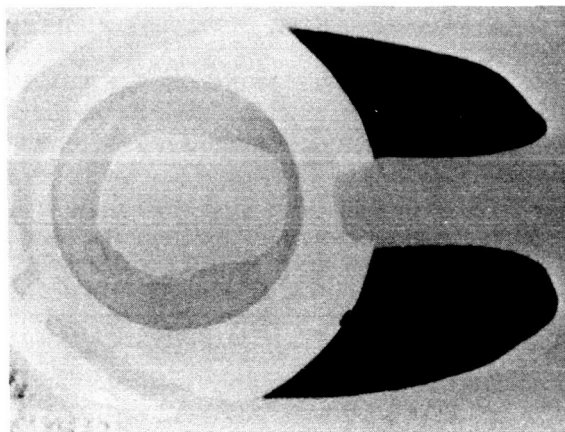Fig. 10. Mariner-9 photograph — Mars crater with bi-lobate pattern.

Fig. 11. Wind tunnel model crater with bi-lobate pattern, $U_\infty^2/gD_c = 6.6$.

205

Figure 12 illustrates the results of a wind tunnel test in which 12 micron diameter copper particles were placed inside a 30 cm crater and the floor was covered with 526 micron diameter sand. A very elongated bi-lobate pattern is observed in the crater wake due to a relatively higher crater rim height. Modeling parameters were $U_\infty^2/gD_c = 22.77$, $U_F/u_{*_t} = 0.078$ and 14.30 for the copper and sand, respectively, $U_\infty/U_{\infty_t} = 0.62$ and 0.86, and $\rho D_c/\rho_p D_p = 3.680$ and 0.283. Similar patterns have been observed behind rocks in snow[34,35].
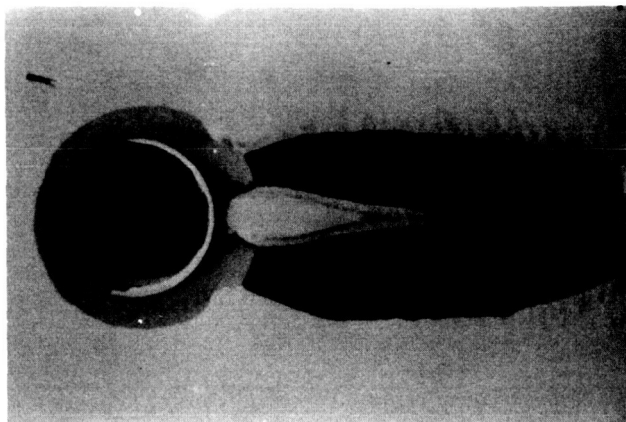

Fig. 12. Wind tunnel model crater with bi-lobate pattern, $U_\infty^2/gD_c = 22.77$.

The modeling parameters in the wind tunnel test pictured in Figs. 13 and 14 were $U_\infty^2/gD_c = 32.8$, $U_F/u_{*_t} = 5.8$, $U_\infty/U_{\infty_t} = 1.195$ ($U_\infty = 803$ cm/sec), and $\rho D_c/\rho_p D_p = 0.525$. Again the bi-lobate pattern is very evident. As time passes, the central region of deposited material erodes away to leave a triangular region of material as shown in Fig. 14.

Fig. 13. Wind tunnel model crater with bi-lobate pattern, $U_\infty^2/gD_c = 32.8$.

Fig. 14. Wind tunnel model crater with triangular deposit region, later in same test as Fig. 13.

Another wind tunnel test in which 91 micron diameter glass spheres were redistributed one cm deep prior to the test is shown in Figs. 15 and 16. Evidence of higher wake velocity is shown here by the fact that the ripple wavelength is longer in the wake than outside. Modeling parameters were $U_\infty^2/gD_c = 5.8$, $U_F/u_{*_t} = 2.4$, $U_\infty/U_{\infty t} = 0.773$ ($U_\infty = 413$ cm/sec), and $\rho D_c/\rho_p D_p = 1.599$.

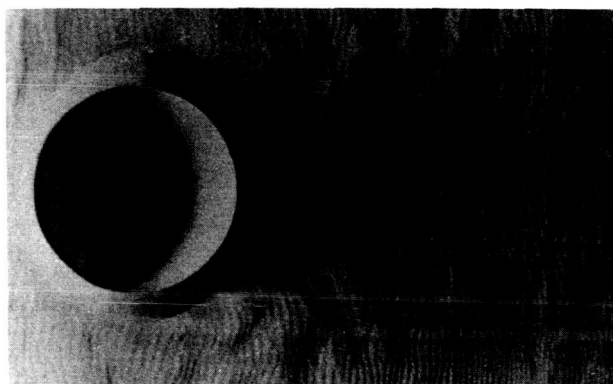

Fig. 15. Wind tunnel model crater showing longer ripple length in wake region, $U_\infty^2/gD_c = 5.8$.
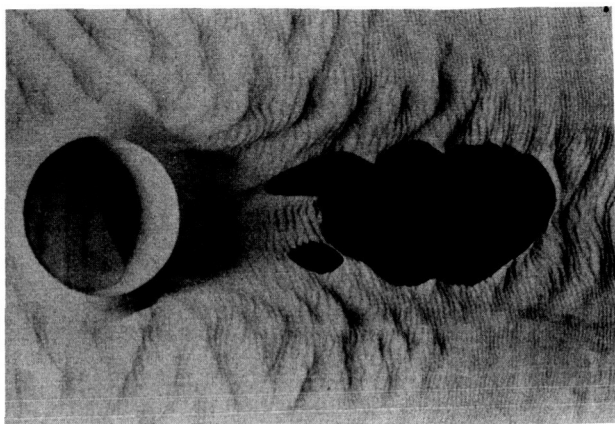
Fig. 16. Wind tunnel model crater, later in same test as Fig. 15.

Figure 17 illustrates the pattern developed for very small diameter particles. The particles are 38 micron diameter glass spheres and are too small to form the ordinary ripple formation[1]. The modeling parameters are U_∞^2/gD_c = 17.85, U_F/u_{*_t} = 0.49, $U_\infty/U_{\infty t}$ = 1.036 (U_∞ = 484 cm/sec), and $\rho D_c/\rho_p D_p$ = 2.606.
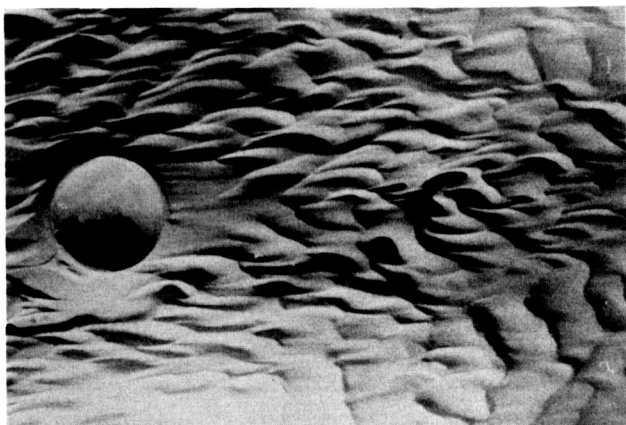

Fig. 17. Wind tunnel model crater, ripple pattern with very small particles, U_∞^2/gD_c = 11.88.

Figure 18 and 19 compare Mariner 9 and wind tunnel photographs in which streamlines curving downstream off the edge of the crater rim can be seen by deposited material patterns in both pictures. Modeling parameters in the wind tunnel were U_∞^2/gD_c = 16.6, U_F/u_{*_t} = 0.08 (12 micron diameter copper particles), $U_\infty/U_{\infty t}$ = 0.53 (U_∞ = 700 cm/sec), $\rho D_c/\rho_p D_p$ = 3.680. In this test the modeling material was placed in the interior of the crater only prior to the test.

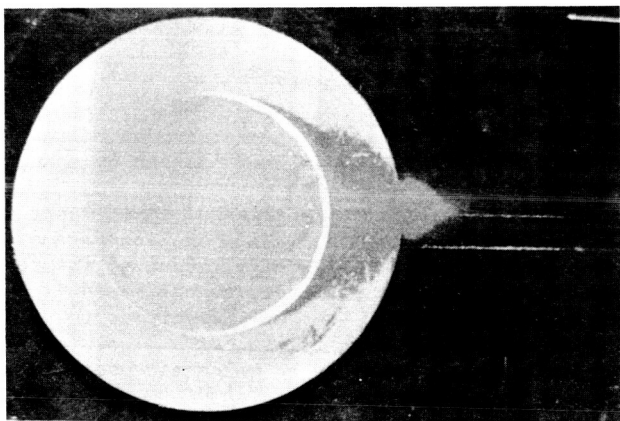Fig. 18. Mariner 9 photograph — Mars crater with lateral curved streaks.

Fig. 19. Wind tunnel model crater with lateral streaks and triangular deposit, $U_\infty^2/gD_c = 16.6$.

Figure 20 illustrates a field test in which a natural snow-storm deposited material over a previously constructed crater (6 m diameter). Triangular deposit regions and cleared wake areas were observed after snowstorms in patterns very similar to the wind tunnel tests. The modeling parameters in this field test were estimated to be $U(h)^2/gD_c = 11$ (based on same relative height h/L in the wind tunnel), $U_F/u_{*t} = 5(\pm 3)$, $\rho D_c/\rho_p D_p \cong 30$, $U(h) = 2530$ cm/sec. In other snowstorms in which similar patterns were obtained, the value of the Froude number ranged down to 0.4.

Fig. 20. Snow deposits in vicinity of 6 meter diameter crater (at upper left).

Although not all modeling parameters can be satisfied in the wind tunnel, a great deal of information can be gained about the nature of the flow field and the resulting depositional and ero-sional features. A systematic series of experiments is currently underway, in which each of the major modeling parameters is varied independently, to determine its effect upon eolian features. This is done by varying crater diameter, tunnel speed, and modeling material. The results will not only enable us to determine effects of each similitude parameter, but will also assist greatly in later numerical experiments in which all modeling parameters can be satisfied.

Acknowledgment

References

1. Bagnold, R. A., <u>The Physics of Blown Sand and Desert Dunes</u>, Methuen, London, 1941.

2. Chepil, W. S., and N. P. Woodruff, "The Physics of Wind Erosion and Its Control," Advances in Agronomy, <u>15</u>, 211-302, 1963.

3. Malina, F. J., "Recent Developments in the Dynamics of Wind-Erosion," Trans. American Geophysical Union, Pt. II, 262, 1941.

4. Ford, E. F., "The Transport of Sand by Wind," Trans. American Geophysical Union, <u>38</u>, 171-174, 1957.

5. Chang, T. S., W. C. Lucas, and W. W. Youngblood, "Laboratory Simulation of the Mars Atmosphere, A Feasibility Study," NASA CR-61168, 1968.

6. Bidwell, J. M., "Notes on Martian Sandstorms," Martin Marietta Corp. Report 1610-68-34, 1965.

7. Adlon, G. L., R. K. Weinberger, and D. R. McClure, "Martian Sand and Dust Storm Simulation and Evaluation," NASA CR-66882, 1969.

8. Hertzler, R. G., "Particle Behavior in a Simulated Martian Environment," McDonnell Aircraft Corporation, Report E418, 1966.

9. Hertzler, R. G., "Behavior and Characteristics of Simulated Martian Sand and Dust Storms," McDonnell Aircraft Corporation, Report E720, 1966.

10. Lumley, J. L., and H. A. Panofsky, <u>The Structure of Atmospheric Turbulence</u>, Wiley, New York, 1964.

11. Plate, E. J., "Aerodynamic Characteristics of Atmospheric Boundary Layers," AEC Critical Review Series, 1971.

12. Jensen, M., "The Model-Law for Phenomena in Natural Wind," Ingeniøren, <u>2</u>, 121, 1958.

13. Cermak, J. E., "Laboratory Simulation of the Atmospheric Boundary Layer," AIAA J., <u>9</u>, 1746, 1971.

14. Davenport, A. G., and N. I. Syumov, "The Application of the Boundary Layer Wind Tunnel to the Prediction of Wind Loading," In <u>Wind Effects on Buildings and Structures</u>, Vol. I, Univ. of Toronto Press, 1968.

211

15. Owen, P. R., and H. K. Zienkiewics, "The Production of Uniform Shear Flow in a Wind Tunnel," J. Fluid Mechanics, 2, 521, 1957.

16. Counihan, C., "An Improved Method of Simulating an Atmospheric Boundary Layer in a Wind Tunnel," Atmospheric Environment, 3, 197, 1969.

17. Sundaram, T. R., G. R. Ludwig, and G. T. Skinner, "Modeling of the Turbulence Structure of the Atmospheric Surface Layer," AIAA J., p. 743-750, 10, 1972.

18. Sagan, C., and J. B. Pollack, "Windblown Dust on Mars," Nature, 223, 791-794, 1969.

19. Strom, G. H., and R. W. Gerdel, "Scale Simulation of a Blowing Snow Environment," Proceedings, Institute Environmental Science, 53, 53-63, 1961.

20. Zingg, A. W., "Wind-Tunnel Studies of the Movement of Sedimentary Material," Proceedings of the Fifth Hydraulics Conference, Bull. 34, Univ. of Iowa Studies in Engineering, 111-135, 1953.

21. Owen, P. R., "Saltation of Uniform Grains in Air," J. Fluid Mechanics, 20, Pt. 2, 225-242, 1964.

22. Snyder, W., "Similarity Criteria for the Application of Fluid Models to the Study of Air Pollution Meteorology," Boundary Layer Meteorology, 3, 113-134, 1972.

23. Bagnold, R., "The Flow of Cohesionless Grains in Fluids," Philosophic Transactions of the Royal Society, A, 249, 239-297, 1956.

24. Bagnold, R. A., "The Nature of Saltation and of 'Bed-Load' Transport in Water," Proceedings of the Royal Society of London, A, 332, 473-504, 1973.

25. Chepil, W. S., "The Use of Evenly Spaced Hemispheres to Evaluate Aerodynamic Forces on a Soil Surface," Transactions American Geophysical Union, 39, 397, 1958.

26. Einstein, H., and E. El-Samni, "Hydrodynamic Forces on a Rough Wall," Reviews of Modern Physics, 21, 520-524, 1949.

27. Schlichting, H., Boundary Layer Theory, McGraw-Hill, N.Y., 1968.

28. Walz, A., Boundary Layers of Flow and Temperature, MIT Press, Cambridge, Mass., 1969.

29. Chepil, W. S., "Equilibrium of Soil Grains at the Threshold of Movement by Wind," Soil Science Society Proceedings, 23, 422-428, 1959.

30. Csanady, G. T., "Geostrophic Drag, Heat and Mass Transfer Coefficients for the Diabatic Ekman Layer," J. Atmospheric Sciences, 29, 488-496, 1972.

31. Sedney, R., "A Survey of the Effects of Small Protuberances on Boundary-Layer Flows," AIAA J., 11, 782-792, 1973.

32. Gregory, N., and W. Walker, "The Effect on Transition of Isolated Surface Excrescences in the Boundary Layer," Great Britain, Aeronautical Research Council, Reports and Memoranda No. 2779, 1951.

33. Hunt, J. C. R., "The Effect of Single Buildings and Structures," Philosophical Transactions of the Royal Society of London, A, 269, 457-468, 1971.

34. Cornish, V., "On Snow-Waves and Snow-Drifts in Canada," The Geographical Journal, 20, 137-173, 1902.

35. Seligman, G., Snow Structure and Ski Fields, MacMillan, London, 1936.